

PACS numbers: 42.30.Wb, 42.25.Kb, 81.70.Fy, 87.57.-s, 87.61.Np, 87.64.-t, 87.85.Lf
DOI: 10.1070/QE2012v042n05ABEH014559

The use of optical coherence tomography for morphological study of scaffolds

B.A. Veksler, V.L. Kuz'min, E.D. Kobzev, I.V. Meglinski

Abstract. **Aimed at possible widening of the optical coherence tomography (OCT) field of application, an attempt is made to use OCT in tissue engineering and cell transplantology as a tool for morphological studies of substrate materials by the example of scaffolds. By means of the traditional fibreoptical OCT scheme the images of inner structure of scaffolds are obtained, and simultaneously the spatial distribution of the intralipid flow velocity is reconstructed using the Doppler OCT. It is shown that combined use of traditional OCT and Doppler OCT schemes allows revealing the regions of the scaffold demonstrating optimal effect of shear stress, which is a key factor of cell growth.**

Keywords: *optical coherence tomography, scaffold, tissue engineering, shear stress.*

1. Introduction

Optical diagnostics methods find new and new application in different biomedical fields, including such as tissue engineering and cell transplantology [1]. To restore a damaged tissue, the regenerative ability of cells, e.g., fibroblasts in skin or chondrocytes in tendon [2] are intensely used. Oriented growth and controlled development of cells is implemented by using scaffolds* [3, 4]. The nutrition of cells, as well as the variation of their proliferation velocity within the scaffold, are realised in the regime of optimal shear stress, artificially created by nutrient microflows [5]. To calculate the optimal morphological properties of a scaffold they usually make use of the Michaelis–Menten equation, describing the processes of nutrient absorption by cells, or the Navier–Stokes equation for modelling liquid microflows in the scaffold [6].

To visualise the microstructure and to execute operational control of nutrient microflows intensity in scaffolds one may use computer tomography methods [7], as well as traditional microscopy [8], commonly used for flow control in biological objects *in situ*, or confocal laser microscopy [9, 10]. The latter is intensely used for morphological studies of biotissue structures with the penetration depth up to 100–150 μm and spatial resolution ~1 μm [11, 12]. However, it should be noted that the multiple scattering of probing radiation, caused by the complex porous structure of scaffolds, substantially limits and strongly hampers their optical diagnostics.

In the present paper we make an attempt to use the optical coherence tomography (OCT) [13–16] and Doppler OCT [11] for simultaneous visualisation of the scaffold inner structure and quantitative analysis of the spatial distribution of microflows within this structure. The OCT allows obtaining structure images of biotissues up to 1.5 mm thick with high spatial resolution (2–15 μm) [17–22]. Moreover, it was shown that OCT combined with the optical immersion technique offers a realistic possibility to increase the probing depth and spatial resolution [23, 24]. It was also demonstrated that Doppler OCT allows quantitative measurement of velocities of the scattering particles (with resolution up to 10 μm s^{-1}) and reconstruction of spatial velocity distribution in complex liquid flows including laminar and turbulent ones [24–26].

2. Basic principles of the OCT method

The principle of OCT operation, consisting in the use of low-coherency optical interferometry, was widely discussed earlier and thoroughly described in a number of publications [14–16]. Therefore, here we present only a brief description of the basic principles of the OCT method and emphasise only some particular aspects of theoretical description of the OCT signal formation, missing in common considerations. In particular, we will consider the time averaging of the registered signal and explicitly describe the contributions, containing the statistical noise and leading to the OCT signal distortion, which, in turn, essentially limits the applicability of the method in practical diagnostics of randomly inhomogeneous media.

The OCT signal is detected as a result of superposition of the fields $E_r(\boldsymbol{r}, t)$ and $E_s(\boldsymbol{r}, t)$ coming from the sample and reference arms of a Michelson interferometer [27], respectively, when under the condition of equality of optical path lengths in both arms within the temporal coherence length of the probing radiation the interference is observed. Thus, in the absence of randomly inhomogeneous medium, when the radi-

* Scaffold is, originally, a temporary metal or wooden framework that is used to support workmen and materials during the erection, repair, etc., of a building or other construction. Now this term is conventional in cell technology practice, where it means natural or artificial framework on the base of substrate materials used for oriented growth of cells. It is used for spatial transplant formation.

B.A. Veksler Cranfield Health, Cranfield University, Cranfield, MK43 0AL, UK;
V.L. Kuz'min Department of Physics, Saint-Petersburg State University, ul. Ulyanovskaya 1, 198504 St.-Petersburg, Russia;
E.D. Kobzev Department of Chemistry, University of Oxford, Oxford, OX4 4BU, UK;
I.V. Meglinski N.G. Chernyshevsky Saratov State University (National Research University), ul. Astrakhanskaya 83, 410012 Saratov, Russia; Cranfield Health, Cranfield University, Cranfield, MK43 0AL, UK; Jack Dodd Centre for Quantum Technology, Department of Physics, University of Otago, Dunedin 9054, New Zealand; e-mail: i.meglinski@cranfield.ac.uk

Received 7 February 2011; revision received 22 February 2012
Kvantovaya Elektronika **42** (5) 394–398 (2012)
Translated by V.L. Derbov

ation in the sample arm of the interferometer is reflected from a mirror, the signal registered by the photodetector may written as [28]:

$$I(z) = \langle I_r \rangle + \langle I_s \rangle + 2\sqrt{\langle I_r \rangle \langle I_s \rangle}\,\mathrm{Re}\{\gamma(\tau)\}. \quad (1)$$

Here $I_r = \langle E_r^*(t+\tau)E_r(t+\tau)\rangle = \frac{1}{2}I_0$ and $I_s = \langle E_s^*(t)\,E_r(t)\rangle$ are the time-averaged intensities of the optical radiation, coming from the reference and sample arms of the interferometer, respectively, and independent of the optical path length difference ΔL between the interferometer arms; I_0 is the intensity of the incident radiation; $\tau = 2z/c$ is the time shift of the interfering fields caused by the additional path difference $2z$; z is the shift of the scanning mirror in the reference arm; c is the speed of light in free space; the angle brackets denote averaging over the observation time.

The temporal coherence function $\gamma(\tau) = \gamma(2z/c)$ contains the dependence on the carrier frequency and the spectrum shape of the radiation source. For a source with a Gaussian spectrum we have

$$\gamma(\tau) = \exp\left[-\left(\frac{\pi\Delta\nu\tau}{2\sqrt{\ln 2}}\right)^2\right]\exp(-2i\pi\bar{\nu}\tau), \quad (2)$$

where $\Delta\nu$ is the total spectral width at the half-maximum of the source function; $\bar{\nu}$ is the carrier frequency. When a sample of a randomly inhomogeneous medium is placed into the sample arm of the interferometer, the particular form of the interference term in Eqn (1) depends on the light scattering model in the sample under study. Thus, in the case of a simple model having only internal boundaries that can partially reflect the probing radiation, Eqn (1) takes the form:

$$I(z) = \langle I_r \rangle + \langle I_s \rangle + 2\sqrt{\langle I_r \rangle \langle I_s \rangle}\,\mathrm{Re}[R(L_s) \otimes \gamma(\tau_s)], \quad (3)$$

where $R(L_s)$ is the fraction of the radiation reflected from an internal boundary located within the studies medium at the depth L_s; $\tau_s = \Delta L/c$ is the radiation delay time caused by the difference $\Delta L = L_s - L_r$ between the optical path lengths in the reference (L_r) and the sample (L_s) arms of the interferometer.

It is necessary to note that besides the reflections from the internal boundaries of the medium each individual scan $I(z)$ is caused by a certain random configuration of scatterers, too. Therefore, in contrast to the first term in Eqn (3), the intensity I_s and the function $\gamma(\tau_s)$ are critically dependent not only on the position of the boundaries within the sample, but also on the configuration of scatterers. The additional phase incursion, determined by the optical path length difference, is responsible for speckle formation. To eliminate the speckles, the scanning procedure is repeated 25–1000 times, which is theoretically equivalent to statistical averaging (see, e.g., [29]).

It is also worth noting that OCT does not allow distinguishing inhomogeneities, whose scale is smaller than the coherence length of the probing radiation

$$l_c = \frac{2c\ln 2}{\pi}\frac{1}{\Delta\nu}. \quad (4)$$

Such inhomogeneities manifest themselves in the form of statistical noise.

Let us present the field in the medium as

$$E_s(\boldsymbol{r}, t) = \overline{E_s(\boldsymbol{r}, t)} + \delta E_s(\boldsymbol{r}, t), \quad (5)$$

where the bar denotes statistical averaging over the small-scale inhomogeneities. The quantity $\delta E_s(\boldsymbol{r}, t)$ is the fluctuating part of the field that determines speckles due to multiple scattering. In a nonscattering transparent medium $\delta E_s(\boldsymbol{r}, t) = 0$, and the interference contribution into the OCT signal is determined by the mean field $\overline{E_s(\boldsymbol{r}, t)}$.

Extracting the statistical averages, we present the intensity in the sample arm as

$$I_s = I_s^0 + 2\mathrm{Re}\langle\overline{E_s(t)}\delta E_s^*(t)\rangle + \langle\delta E_s(t)\delta E_s^*(t)\rangle. \quad (6)$$

In the case of a single-layer medium the mean intensity of light is

$$I_s^0 = \frac{1}{2}R_F^2 I_0 \exp\left(-\frac{2d}{l}\right), \quad (7)$$

where R_F is the Fresnel coefficient of reflection from the far boundary of the medium; d is the layer thickness; l is the photon mean free path in the medium, or the extinction length. The quantity I_s^0 is constant and small because of strong damping due to double passing (forth to the boundary and back) of light through the medium layer. The term $2\mathrm{Re}\langle\overline{E_s(t)}\delta E_s^*(t)\rangle$, linear in field fluctuations, is practically not observable because of random phase shifts. The form $\langle\delta E_s(t)\delta E_s^*(t)\rangle$, quadratic in fluctuations, determines the dominant contribution into speckles. Its statistical average, i.e., the average over small-scale inhomogeneities,

$$D = \overline{\langle\delta E_s(t)\delta E_s(t)\rangle}, \quad (8)$$

represents the speckle variance [30], and its root-mean-square deviation $\sigma = \sqrt{D}$ is the speckle mean value. The interference term is

$$2\mathrm{Re}\langle E_r^*(t+\tau)E_s(t)\rangle = 2\mathrm{Re}\langle E_r^*(t+\tau)\overline{E_s(t)} + E_r^*(t+\tau)\delta E_s(t)\rangle. \quad (9)$$

Optical properties of real biological media essentially differ from those of idealised models used in theoretical analysis [31]. Nevertheless, the principal estimates of the validity limits for the medium, considered in the present paper, remain true. The amplitude of the detected OCT signal appears to be proportional to the stepwise change in the refractive index at the interface between the media or at the boundaries of the medium structure elements, located at the depth, corresponding to the optical path length in the reference arm. In this way the depth-resolved probing of the medium that yields the location of the refractive index step is accomplished.

It should be noted that the stepwise change in the refractive index may be inherent in different objects and inhomogeneities within the medium, including planar boundaries between its layers, macro- and micro-inhomogeneities, as well as ensembles of light-scattering particles having the dimensions essentially smaller than the probing beam width. Depending on the inhomogeneity type, the stepwise changes of refractive index manifest themselves in the registered OCT signal (so-called A-scan) in a different way. The image of the layer interface or the contours of a macroscopic inhomogeneity can be observed under the condition that the interfaces are perpendicular to the direction of probing. Moreover, multiple scattering greatly affects the OCT signal formation and the limitation of the probing depth [32].

The detection of the velocity of scattering particles, implemented using the OCT scheme, is based on measuring the central frequency shift of the Doppler signal, caused by directed motion of particles, localised within the scaffold. Using the singe-scattering approximation, one can express the velocity of moving particles in a straight-channel laminar flow as [27]

$$\left|V_{\mathrm{D}}\right|_z = \frac{f_{\mathrm{D}}\lambda_0}{2n\cos\alpha}, \tag{10}$$

where f_{D} is the central frequency of the Doppler signal; λ_0 is the incident radiation wavelength; α is the angle between the flow velocity vector and the direction of propagation of the probing radiation. However, in the case of scaffolds the shape of the cross section of channels is irregular, and the direction of the flow velocity vector is variable. Besides, due to multiple light scattering by the intralipid particles, the wave vector of the probing radiation also becomes differently directed. Hence, the angle α in the above expression becomes ill-defined, due to which the spectrum of Doppler frequency shifts acquires an irregular shape.

In this case the Doppler shift is estimated by comparison of sequentially measure A-scans and is presented in the form [33]

$$f_{\mathrm{D}} = \frac{1}{2\pi T}\tan^{-1}\left\{\frac{\Im\left[N^{-1}\sum_{j=1}^{N}\tilde{S}_j(z,T)\tilde{S}^*_{j+1}(z,T)\right]}{\Re\left[N^{-1}\sum_{j=1}^{N}\tilde{S}_j(z,T)\tilde{S}^*_{j+1}(z,T)\right]}\right\}, \tag{11}$$

where $\Im$ and $\Re$ are the real and imaginary part of the product of complex conjugate functions $\tilde{S}_j(z,T)$ and $\tilde{S}^*_j(z,T)$, respectively, corresponding to sequentially measured A-scans; the asterisk denotes a complex conjugate operator; T is the time interval between two adjacent A-scans j and $j+1$; N is the number of A-scans used for averaging.

3. Materials and methods

For morphological studies of the scaffold internal structure we used the OCT setup based on the fibreoptical Michelson interferometer (Fig. 1). The low-coherence optical radiation from a superluminescent diode SLD with the central wavelength $\lambda_0 = 1298$ nm, $\Delta\lambda = 52$ nm and the output power 0.5 mW (Superlum, Russia) is split into two equal components, one of which is directed into the sample arm of the interferometer and the other one into the reference arm. Matched orificing of radiation from the SLD source and the PD1 photodetector visual field by means of an optical fibre in combination with small coherence length of the probing radiation (20–30 μm) allows localisation of the measurement region in a small volume (8–50 μm^3). Moreover, this optical system allows practically instantaneous depth scanning of the studied medium implemented via moving the corner reflector CR in the reference arm of the interferometer.

As a result the amplitude of the signal detected by the photodetector varies proportional to the stepwise changes of the refractive index of structure elements of the studied sample, thus making it possible to reconstruct the depth spatial distribution of the inhomogeneity boundaries. The photodetector PD2 registers the interference signal, produced by the radiation coming from the reference and sample arms of the interferometer. Thus 130000 digital readings are obtained, or one reading per 1 μs. However, in this work only 40000 readings were used, which corresponds to the scaffold fragment

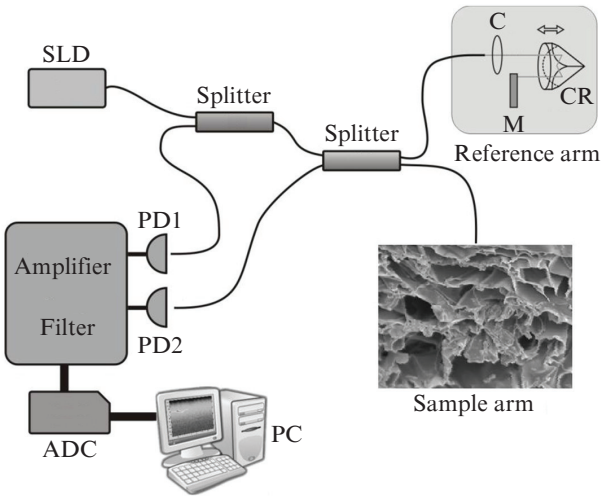

Figure 1. Traditional scheme of the fibreoptic OCT: (SLD) superluminescent diode; (PD1, PD2) photodetectors; (CR) corner reflector; (C) collimator; (M) fixed mirror; (ADC) analogue-to-digital convertor, the data acquisition unit; (PC) personal computer.

having the width ~1.5 mm. In the course of OCT imaging of the internal structure of the scaffold the averaging over 20 A-scans was performed for each of 80 points on the scaffold surface; the total time of obtaining one image amounted to ~64 s.

The used Doppler modification of the OCT, earlier implemented and thoroughly presented in [24, 25], allows detection of the flow velocity of the scattering particles, moving inside the sample, within the limits of ±65 mm s^{-1}. Measurements of the microscopic flow velocity are carried out at the same experimental OCT setup (Fig. 1) by means of applying the fast Fourier transform [25].

The studied scaffolds were made of the polysaccharide polymer chitosan [19]. Two-percent solution of this substance, obtained by dissolving chitosan particles in one-percent water-free acetic acid, was placed into cylindrical moulds 1.5 mm in diameter and frozen during a few hours with following sublimation. After gradient rehydration with ethanol (100%, 70%, and 50%), the scaffolds synthesised in this way (Fig. 2) were placed into saline.

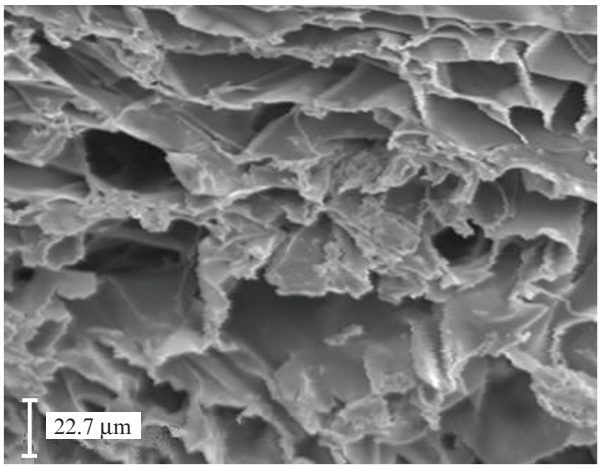

Figure 2. Microphotography of internal structure of a scaffold obtained using a scanning electron microscope (ISI ABT-55, Great Britain).

To model the cells and the nutrient liquid, supplied to the cell structures within the scaffold, we used one-percent aqueous solution of intralipid (10%, Sigma-Aldrich, Great Britain), presenting an aqueous emulsion of phospholipid micelles with the diameters distributed according to the normal law with the maximum at 300 μm. The choice of this solution as a model liquid is caused by the fact that its optical properties are in good agreement with those of biotissue cells [34]. The intralipid supply was implemented using a syringe pump (Harward, mod. 975, Great Britain) providing a stable laminar flow at the scaffold entry with the maximal velocity of 16 mm s^{-1}.

4. Discussion of results

The obtained OCT image of the inner side of the scaffold is presented in Fig. 3. According to the results of electron microscopy (see Fig. 2) the mean inhomogeneity size in the scaffold appears to be comparable with the coherence length of the probing radiation, i.e., 20–30 μm. Due to this reason, as well as to equalising of the refractive index of the structure elements of the scaffold and the intralipid aqueous solution filling it, the porous structure, well seen in the microphotograph (Fig. 2), in the OCT images can be recognised only in the near-surface layers. With the growth of depth the porosity of the scaffold structure becomes poorly visible or vanishes. The spatial transverse distribution of microflows of the liquid in the scaffold (Fig. 4), obtained by means of Doppler OCT, shows that the liquid flow is essentially hampered or completely absent. The latter is, apparently, caused by the fact that the size of lipid particles, present in the intralipid solution, considerably exceeds the diameter of the scaffold pores, which leads to blocking of pores and partial or total stopping of the liquid flows. In this connection the intralipid solution was twice filtered using embossed filtering paper (density 78 g m^{-2}, thickness 0.17 mm, size of pores 15 μm), and the experiment was repeated with the new filtered solution.

The results presented in Fig. 5 show that after filtration of the intralipid the spatial transverse velocity distribution of the arising microflows appears to be strongly nonuniform, with high (up to ±5 mm s^{-1}) velocity fluctuations. As shown in [35], the comparison of the structure OCT image of the scaffold (Fig. 3) and the spatial distribution of microflow velocities, obtained using the Doppler OCT (Fig. 5), allows depth monitoring of the produced shear stress in the given region of the scaffold and, hence, optimisation of the nutrient liquid supply.

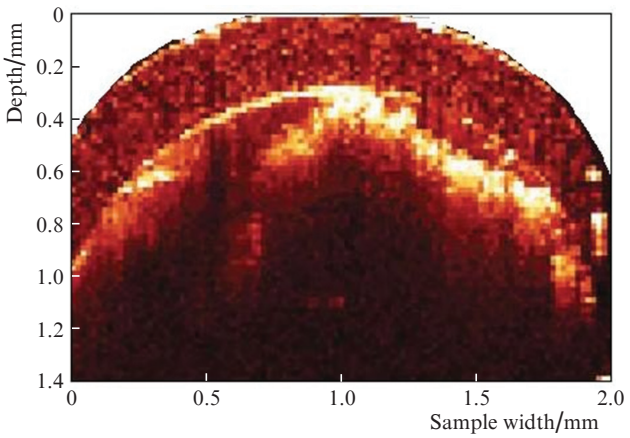

Figure 3. OCT image of the inner structure of the scaffold.

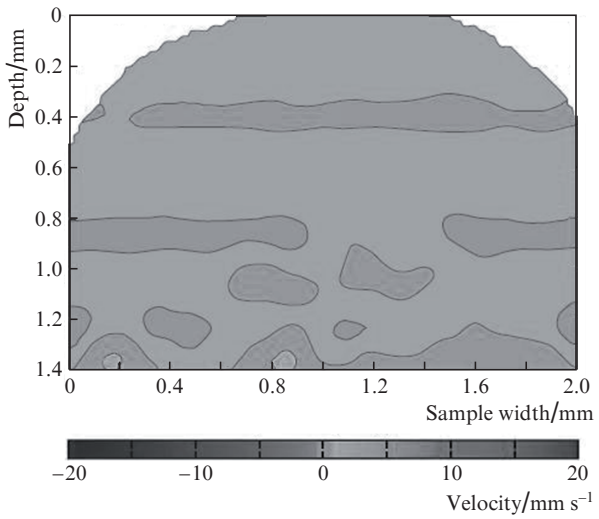

Figure 4. Spatial distribution of the intralipid microflow velocity in the scaffold, obtained using Doppler OCT.

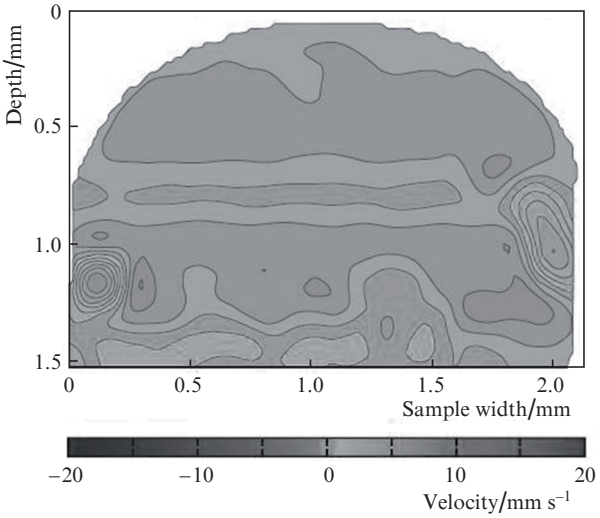

Figure 5. Spatial transverse distribution of the microflow velocity of filtered intralipid in the scaffold.

5. Conclusions

Time averaging of the registered signal is considered and the principal causes of the OCT signal distortion are indicated. On the base of a model experiment the practical possibility of using OCT for solving the problems of tissue engineering and cell transplantology is demonstrated. The study of the internal structure of scaffolds is implemented on the basis of the conventional fibreoptic OCT scheme. At the same time using the Doppler OCT the spatial distribution of intralipid microflows in the scaffold was determined. It is shown that combined use of the OCT and its Doppler modification really allows detection of the substrate regions with the optimal effect of shear stress, which is a mechanical factor of cell growth. It is expected that the present approach in combina-

tion with computer modelling will allow substantial improvement of the quality of scaffold fabrication and optimisation of nutrient supply and oriented cell growth.

Acknowledgements. The work was partially supported by the BBSRC (Project No. BBS/B/04242, Great Britain). The authors express their deep gratitude to Dr. Marco Bonesi (Medical University of Vienna, Austria) for useful advice and help in preparing the experiments.

References

1. Minuth W.W., Strehl R., Schumacher K. *Tissue Engineering: From Cell Biology to Artificial Organs* (Berlin: Wiley-VCH, 2006).
2. Langer R., Vacanti J.P. *Science*, **260**, 920 (1993).
3. Temenoff J.S., Lu L., Mikos A.G. *Bone Tissue Engineering Using Synthetic Biodegradable Polymer Scaffolds* (Toronto: Em Squared Inc., 2000).
4. Mikos A.G., Temenoff J.S. *Electron. J. Biotech*., **3**, 114 (2000).
5. Lin M.-C., Almus-Jacobs F., Chen H.-H., Parry G.C.N., Mackman N., Shyy J. Y.-J., Chien S.J. *Clin. Invest*., **99**, 737 (1997).
6. Chung C.A., Chen C.W., Chen C.P., Tseng C.S. *Biotechnol. Bioeng*., **97**, 1603 (2007).
7. Cioffi M., Boschetti F., Raimondi M.T., Dubini G. *Biotechnol. Bioeng*., **93**, 500 (2006).
8. Stephens J.S., Cooper J.A., Phelan F.R., Jr., Dunkers J.P. *Biotechnol. Bioeng*, **97**, 952 (2007).
9. Pawley J.B. *Handbook of Biological Confocal Microscopy* (Berlin: Springer, 2006).
10. Ren F., Smith I.O., Baumann M.J., Case E.D. *Int. J. Appl. Ceram. Tech*., **2**, 200 (2005).
11. Tuchin V.V. *Opticheskaya biomeditsinskaya diagnostika* (Optical Biomedical Diagnostics) (Moscow: Fizmatlit, 2007).
12. Meglinskii I.V., Bashkatov A.N., Genina E.A., Churmakov D.Yu., Tuchin V.V. *Kvantovaya Elektron*., **32**, 875 (2002) [*Quantum Electron*., **32**, 875 (2002)].
13. Huang D., Swanson E.A., Lin C.P., Schuman J.S., Stinson W.G., Chang W., Hee M.R., Flotte T., Gregory K., Puliafito C.A., Fujimoto J.G. *Science*, **254**, 1178 (1991).
14. Schmitt J.M. *IEEE J. Sel. Top. Quantum Electron.,* **5**, 1205 (1999).
15. Fercher A.F., Drexler W., Hitzenberger C.K., Lasser T. *Rep. Progr. Phys*., **66**, 239 (2003).
16. Gladkova N.D., Sergeev A.M. *Rukovodstvo po opticheskoy kogerentnoy tomografii* (Manual in Optical Coherence Tomography) (Moscow: Fizmatlit, 2007).
17. Kuranov R.V., Sapozhnikova V.V., Shakhova N.M., Gelikonov V.M., Zagaynova E.V., Petrova S.A. *Kvantovaya Elektron*., **32**, 993 (2002) [*Quantum Electron*., **32**, 993 (2002)].
18. Kirillin M.Yu., Priezzhev A.V., Tuchin V.V., Wang R.K., Myllyla R. *J. Phys. D: Appl. Phys*., **38**, 2582 (2005).
19. Bagnaninchi P.O., Yang Y., El Haj A., Hinds M.T., Wang R.K. *Proc. SPIE Int. Soc. Opt. Eng*., **6439**, 6430H (2007).
20. Gelikonov V.M., Gelikonov G.V. *Kvantovaya Elektron*., **38**, 634 (2008) [*Quantum Electron*., **38**, 634 (2008)].
21. Zimnyakov D.A., Tuchin V.V. *Kvantovaya Elektron*., **32**, 10 (2002) [*Quantum Electron*., **32**, 10 (2002)].
22. Meglinski I.V., Buranachai C., Terry L.A. *Laser Phys. Lett*., **7**, 307 (2010).
23. Proskurin S.G., Meglinski I.V. *Laser Phys. Lett*., **4**, 824 (2007).
24. Bonesi M., Proskurin S.G., Meglinski I.V. *Laser Phys*., **20**, 891 (2010).
25. Bonesi M., Churmakov D., Meglinski I. *Measur. Sci. Technol*., **18**, 3279 (2007).
26. Bonesi M., Churmakov D.Y., Ritchie L.J., Meglinski I.V. *Laser Phys. Lett*., **4**, 304 (2007).
27. Bouma B.E., Tearney G.J. *Handbook of Optical Coherence Tomography* (New York: Marcel Dekker, 2002).
28. Tomlins P.H., Wang R.K. *J. Phys. D: Appl. Phys*., **38**, 2519 (2005).
29. Karamata B., Laubscher M., Leutenegger M., Bourquin S., Lasser T., Lambelet P. *J. Opt. Soc. Am. A*, **22**, 1369 (2005).
30. Kuz'min V.L., Meglinskii I.V. *Zh. Eksp. Teor. Fiz*., **132**, 323 (2007) [*JETP*, **105**, 285 (2007)].
31. Meglinskii I.V. *Kvantovaya Elektron*., **31**, 1101 (2001) [*Quantum Electron*., **31**, 1101 (2001)].
32. Kirillin M.Yu., Meglinskii I.V., Priezzhev A.V. *Kvantovaya Elektron*., **36**, 247 (2006) [*Quantum Electron*., **36**, 247 (2006)].
33. Zhang J., Chen Z. *Opt. Express*, **13**, 7449 (2005).
34. Flock S.T., Jacques S.L., Wilson B.C., Star W.M., van Gemert M.J.C. *Laser Surg. Med*., **12**, 510 (1992).
35. Van Leeuwen T.G., Kulkarni M.D., Yazdanfar S., Rollins A.M., Izatt J.A. *Opt. Lett*., **24**, 1584 (1999).